



RESEARCH ARTICLE | FEBRUARY 10 2023

## Shedding light on the metal-phthalocyanine EXAFS spectra through classical and *ab initio* molecular dynamics

Gema Raposo-Hernández ; Enrique Sánchez Marcos ; Rafael R. Pappalardo ; José M. Martínez  



*J. Chem. Phys.* 158, 064110 (2023)

<https://doi.org/10.1063/5.0135944>

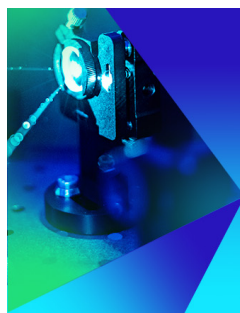


View  
Online



Export  
Citation

CrossMark



The Journal of Chemical Physics  
Special Topic: Time-resolved  
Vibrational Spectroscopy

Submit Today



# Shedding light on the metal-phthalocyanine EXAFS spectra through classical and *ab initio* molecular dynamics

Cite as: J. Chem. Phys. 158, 064110 (2023); doi: 10.1063/5.0135944

Submitted: 23 November 2022 • Accepted: 24 January 2023 •

Published Online: 10 February 2023



View Online



Export Citation



CrossMark

Gema Raposo-Hernández,  Enrique Sánchez Marcos,  Rafael R. Pappalardo,  and José M. Martínez<sup>a)</sup> 

## AFFILIATIONS

Departamento de Química Física, Universidad de Sevilla, 41012 Seville, Spain

<sup>a)</sup> Author to whom correspondence should be addressed: josema@us.es

## ABSTRACT

Extended X-Ray Absorption Fine Structure (EXAFS) theoretical spectra for some 3d transition metal-phthalocyanines—FePc, NiPc, CuPc, and ZnPc—are presented. Their complexity and rigidity make them a good testbed for the development of theoretical strategies that can complement the difficulties present in the experimental spectrum fitting. Classical and *ab initio* molecular dynamics trajectories are generated and employed as a source of structural information to compute average spectra for each MPc species. The original ZnPc force field employed in the classical molecular dynamics simulations has been modified in order to improve the agreement with the experimental EXAFS spectrum, and the modification strategy—based on MP2 optimized structures—being extended to the rest of MPcs. Both types of trajectories, classical and *ab initio*, provide very similar results, showing in all cases the main features present in the experimental spectra despite the different simulation timescales employed. Spectroscopical information has been analyzed on the basis of shells and legs contributions, making possible the comparison with the experimental fitting approaches. According to the simulations results, the simple relationships employed in the fitting process to define the dependence of the Debye Waller factors associated with multiple scattering paths with those of single scattering paths are reasonable. However, a lack of multiple backscattering paths contributions is found due to the intrinsic rigidity of the chemical motif (macrocycle). Its consequences in the Debye Waller factors of the fitted contributions are discussed.

Published under an exclusive license by AIP Publishing. <https://doi.org/10.1063/5.0135944>

## I. INTRODUCTION

Phthalocyanines (H<sub>2</sub>Pcs), as well as many metal substituted phthalocyanines (MPcs), are planar, aromatic macro-cycles, consisting of four isoindole units, joined by four nitrogen atoms, resulting in a tetradentate ligand. Phthalocyanines have an important role in the field of material science and nanotechnology because of their electrical properties and their strong absorption in the visible region. In addition, they are thermally and chemically stable and can support intense electromagnetic radiations.<sup>1–6</sup>

The size of the MPcs depends on the size of the coordinated central atom, which varies within quite a wide range of values.<sup>7–9</sup> The standard oxidation state of Pc is –2, but the oxidation state of the central atom can go from +1 to +5, so, it results in a wide variety of possible structures.<sup>10</sup>

Due to the known *macrocycle effect*<sup>11,12</sup> and the high conjugation (18 $\pi$  electrons, aromatic system), MPc complexes exhibit a quite rigid structure despite their large size, which has been extensively studied by various techniques, such as XPS, X-ray absorption spectroscopy (XAS), and STM.<sup>13–16</sup>

The characterization technique on which this work will focus is *Extended X-ray Absorption Fine Structure* (EXAFS) spectroscopy. This technique is extremely sensitive to the coordination environment of the absorber atom.<sup>17</sup> It is especially relevant in the case of structural determination of species in disordered systems, such as solution or non-crystalline media, since it does not require long-range order.<sup>18</sup>

The XAS spectra of solid FePc, NiPc, CuPc, and ZnPc metal-phthalocyanines have been reported.<sup>19–21</sup> In addition, Carrera *et al.*<sup>19</sup> also measured 0.1M aqueous solution of CuPc at 300 K, obtaining almost the same results, except for the first coordination shell

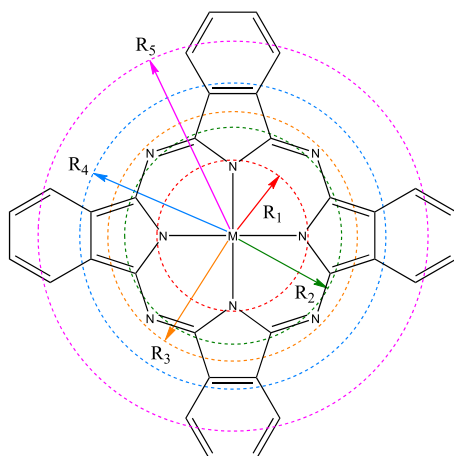


**FIG. 1.** Metal phthalocyanine structure with a schematic representation of the first five shells in dotted lines ( $R_n$ ).

contribution, which has a smaller Debye-Waller factor in solution. Thus, MPcs EXAFS spectra can be well described using only intramolecular scattering contributions, neglecting intermolecular ones (see Fig. 1 for shells definition).

The aim of the present study is the use of theoretical strategies<sup>22–25</sup> for the generation of EXAFS spectra based on structures obtained from molecular dynamics (MD) simulation trajectories. In the context of classical MD and in order to take into account the intramolecular dynamics, a flexible force field being able to describe the molecular vibrations becomes compulsory. This way of generating spectra is especially interesting, since it allows the checking of the goodness of the force field.

There are some published classical force fields for MPcs. Of them is the one published by Shao *et al.*,<sup>26</sup> who developed a Hybrid-COMPASS force field for the CuPc. Dwyer *et al.*<sup>27</sup> reported a new set of force fields within the CHARMM parameterization model, specific to perfluoro-modified MPcs. In particular, our interest relies on the one parameterized for ZnPc. We choose the second force field because its implementation in the employed MD code was easier. Within this force field, by introducing some modifications, it is intended to extend it to the other 3d metals (Fe, Ni, and Cu) in order to generate their corresponding theoretical spectra.

Additionally, *ab initio* molecular dynamics (AIMD) simulations have also been performed in order to compare with the classical results. This way of running simulations offers an alternative to the use of classical force fields, but it has the disadvantage of the large amount of computational cost, and it is also conditioned by the level of theory and the size of the basis sets used. Nonetheless, AIMD results are also reported in this work, allowing the comparison of both theoretical strategies.

Finally, it is worth mentioning that one advantage of the theoretical methodology employed here is the fact that no fitting is performed in the process. Therefore, the number of scattering contributions can be as large as needed. This opens the possibility of analyzing the experimental strategies followed when performing the

EXAFS fitting, i.e., whether the approximations adopted in terms of the chosen scattering contributions and their respective amplitudes agree with the known theoretical results or not. This is particularly relevant when dealing with rather rigid and large structures such as MPcs.

## II. METHODOLOGY

### A. Quantum mechanical computations

The structures of the 3d transition-metal phthalocyanines were optimized at the MP2 level, using 6-311G(d, p)<sup>28–30</sup> basis sets. Charge fitting was done according to the Merz–Singh–Kollman scheme,<sup>31,32</sup> using UFF radii for atomic charge calculations (MKUFF).

Due to the high computational cost of Born–Oppenheimer molecular dynamics (BOMD) simulations, we cannot use the MP2 level of theory. We tested the TPSS<sup>33</sup> functional with the same basis sets of MP2 calculations (6-311G(d, p)). The validity of the functional has been previously proven for metals of the 3d, 4d, and 5d transition series, reproducing properly the experimental geometries and vibration frequencies.<sup>34</sup> The results of the geometry optimization at both levels of theory are collected in Table I. The calculations were performed using ORCA.<sup>35</sup> The differences between both levels of theory are in the hundredth of an angstrom, which we consider to be acceptable for the aim of this work.

### B. Classical molecular dynamics simulation details

Classical Molecular Dynamics (MD) simulations were performed using a modified version of the DLPOLY Classic package.<sup>36</sup> The simulations were run at temperatures of 80 and 300 K in the canonical (NVT) ensemble, using a Nosé–Hoover thermostat with  $\tau = 100.0$  fs. The chosen temperatures match the experimental conditions. No cutoff radius was applied to non-bonding interactions.

The total simulation time was 1.1 ns, with a chosen time step of 0.25 fs. There was a first stage of equilibration lasting for 0.1 ns. The production period was extended for 1 ns, saving configurations every 8000 steps, obtaining trajectories of 500 snapshots. Another set of simulations were run with a production time of 5 ps, saving configurations every 40 steps, obtaining trajectories with 500 snapshots. The aim of these shorter simulations is to compare their results with the BOMD ones.

**TABLE I.** Distances for the first four shells of MPcs from QM-optimizations. See Fig. 1 for shell definition.

(Å)		FePc	NiPc	CuPc	ZnPc
R <sub>1</sub>	MP2	1.936	1.888	1.946	1.985
	TPSS	1.933	1.904	1.958	1.995
R <sub>2</sub>	MP2	2.966	2.934	2.971	2.997
	TPSS	2.977	2.954	2.985	3.011
R <sub>3</sub>	MP2	3.377	3.363	3.379	3.390
	TPSS	3.383	3.374	3.387	3.396
R <sub>4</sub>	MP2	4.207	4.174	4.213	4.240
	TPSS	4.211	4.189	4.225	4.253

### C. Born–Oppenheimer molecular dynamics

The *ab initio* trajectories are computed using ORCA<sup>35</sup> at TPSS/6-311G(d, p).<sup>28–30</sup> Strictly, these are Born–Oppenheimer molecular dynamics (BOMD) simulations because they approximately solve the time-independent Schrödinger equation to compute gradients and then move the atoms according to them.

For each complex, the simulations were run at 80 or 300 K in the NVT ensemble. A first equilibration run of 1 ps was done using the Berendsen thermostat,<sup>37</sup> with a coupling constant of 10.0 fs. The production time was 5 ps using the Nosé–Hoover chain thermostat,<sup>38,39</sup> with a chain length of 3 and a coupling constant of 100.0 fs. The chosen time step was 0.25 fs for both equilibration and production runs. The center of mass was kept fixed in order to avoid drifts.

### D. Modifications introduced in the force field

Some modifications were included in the original force field published by Dwyer *et al.*<sup>27</sup> in order to reproduce the MP2 quantum-optimized geometries. The modified parameters correspond to four equilibrium bond lengths and an equilibrium bond angle, as is shown in Fig. 2 and collected in Table II. The modified parameters correspond to the central region, which is most affected by the substitution of the cation.

In addition, the charges corresponding to the metal and the nearest nitrogen atoms are changed when the central atom is replaced by another 3d transition metal. To do so, the total charge of the M + 4N unit remains as  $-1.719e^-$ , as schematized in Fig. 2, but a redistribution of charge density is done. The values are collected in Table S1 in the [supplementary material](#). Keeping this value in all MPCs avoids the need to reassign charges to the outer atoms of the complex. For this aim, the MKUFF charges obtained from the MP2 calculation are used to compute the  $q_M/q_{Zn}$  ratio (with M = Fe, Ni, and Cu), which is then applied to the charge of Zn atom in the original FF. The charge of nitrogen atoms is then calculated as a difference between the total charge of the region ( $-1.719e^-$ ) minus the metal charge, and divided by 4.

### E. EXAFS spectrum computation

The general formula for the EXAFS spectrum can be expressed as a sum of the contributions to the total amplitude  $\chi(k)$  by each backscattering path,<sup>17,40</sup>

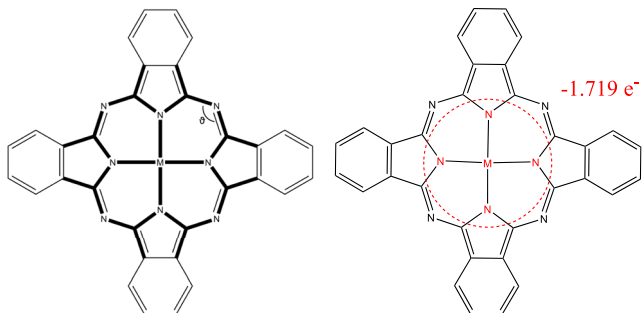


**FIG. 2.** On the left, modified (bold) bonds and angle. On the right, in red, the central atoms of the complex, whose charges are modified. This region remains in all cases with a net charge of  $-1.719 e^-$  after modifications.

$$\chi(k) = \sum_j \frac{N_j}{k\bar{R}_j^2} S_0^2 |F_j^{eff}(k)| e^{-2k^2\sigma_j^2} e^{-\frac{2R_j}{\lambda(k)}} \sin(2k\bar{R}_j + \varphi_j(k)), \quad (1)$$

where, for each backscattering path  $j$ ,  $N_j$  is the coordination number,  $F_j^{eff}$  the backscattering amplitude function,  $S_0^2$  is the amplitude reduction factor,  $\bar{R}_j$  is the mean path distance,  $\varphi_j$  is the phase shift,  $\lambda$  is the photoelectron mean free path, and  $\sigma_j^2$  is the Debye–Waller factor of path  $j$ .

In this work, theoretical EXAFS spectra of the metal K-edge for the different phthalocyanines have been computed, using a set of snapshots extracted from both MD simulations—classical and Born–Oppenheimer. 500 evenly spaced configurations were extracted from the trajectory to assure the convergence.

In order to generate the theoretical EXAFS spectra, the global EXAFS spectrum,  $\bar{\chi}(k)$ , is computed by averaging all the individual spectra obtained for each snapshot:

$$\bar{\chi}(k) = \frac{1}{N_s} \sum_l \chi_l(k), \quad (2)$$

where  $\chi_l(k)$  is the individual spectrum of each snapshot, and  $N_s$  is the total number of snapshots.

Following this strategy, the classical EXAFS equation can be modified according to the expression<sup>22–25</sup>

$$\bar{\chi}(k) = \frac{1}{N_s} \sum_l \sum_j \frac{S_0^2 F_j^{eff}(k)}{kR_{lj}^2} e^{-\frac{2R_{lj}}{\lambda(k)}} \sin(2kR_{lj} + \varphi_j(k)), \quad (3)$$

where  $N_s$  is the number of snapshots, index  $l$  identifies each of them, and  $j$  runs over all the scattering paths considered in each structure. In Eq. (3), the structural disorder arises from the summation over all spectra of the different structures, instead of using a model structure with associated Debye–Waller factors.

Theoretical estimations of the Debye–Waller factors have been obtained through the expression

$$\sigma_i^2 = \left\langle \left( r_i^{eff} - \langle r_i^{eff} \rangle \right)^2 \right\rangle, \quad (4)$$

i.e., the variance of the effective path distance. The effective path distance in a given configuration is defined as the half-length of the full photoelectron path

$$r_i^{eff} = \frac{1}{2} r_i.$$

Therefore, in the case of single scattering contributions, the path distance coincides with the distance between both atoms (absorber and back-scatterer), while for multiple scattering paths, the effective distance is half the sum of each leg distance.

EXAFS calculations for each snapshot were performed with the FEFX code (version 9.6).<sup>41</sup> The Hedin–Lundqvist potential was used to compute the electron density distribution within a self-consistent-field (SCF) approach. Hydrogen atoms were included to calculate the potential, but they were not included as backscattersers.<sup>19,42–44</sup>

After studying the convergence, the cutoff radius around the absorber atom was set to 6 Å, and the multiple scattering paths were extended up to six legs. The  $\Delta E_0$  and  $S_0^2$  were chosen for each MPC to match the most intense oscillation of the experimental EXAFS

**TABLE II.** Modifications included in the equilibrium parameters.

Term	Original ZnPc FF <sup>27</sup>	FePc	NiPc	CuPc	ZnPc
$b_{0(M-N1)}$ (Å)	1.9400	1.9220	1.8369	1.9359	2.0060
$b_{0(N1-C1)}$ (Å)	1.3847	1.3840	1.3780	1.3810	1.3830
$b_{0(N2-C1)}$ (Å)	1.3310	1.3476	1.3435	1.3450	1.3460
$b_{0(C1-C2)}$ (Å)	1.4592	1.4500	1.4505	1.4525	1.4535
$\theta_{0(C1-N2-C1)}$ (°)	125.3075	120.3075	119.3075	120.3075	120.3075

spectrum. The values are collected in Table S2 in the [supplementary material](#). The  $k$  range employed was 2.0–13.0 Å<sup>-1</sup>, and all the spectra were  $k^3$ -weighted.

### III. RESULTS AND DISCUSSION

#### A. Previous experimental results

In the present study, theoretical results are compared with the published experimental EXAFS spectra. The experimental information, as well as the details of the fittings, was extracted from the works of Carrera *et al.*,<sup>19</sup> Rossi *et al.*,<sup>20</sup> and Hong *et al.*<sup>21</sup> The studies agree that the EXAFS spectra of MPcs are well described, using only backscattering paths involving a single molecule. Paths involving other MPc molecules or solvent molecules are found to have negligible contributions compared to those involving intramolecular atoms.<sup>19</sup> The considered backscattering paths employed in the experimental fittings are illustrated in Fig. 3.

The difficulty of the experimental fitting arose when Carrera *et al.* considered the SS1-SS4, MS1-MS3, and MS5-MS8 paths in their fitting, while Rossi *et al.* took into account paths SS1-SS4 and MS1, MS2, MS4, MS5, MS7, and MS8. Furthermore, Hong *et al.* only

considered four single scattering paths, SS1-SS4. Thus, there are different views among the authors on the more relevant paths to be used in the EXAFS fitting.

Regarding the calculation of the DW factors, each path has associated its own DW factor. In principle, it would be necessary to fit all of them, considering a large number of parameters –highly correlated–for each backscattering path. To simplify the problem, it is common to relate the MS DW factors with those of SS according to the so-called *independent vibration model*.<sup>45,46</sup> According to this model, the fittings are performed with the following DW factor relations to reduce the number of free parameters:

$$\sigma_{MS1}^2 = \sigma_{MS2}^2 = 2\sigma_{SS1}^2, \quad (5a)$$

$$\sigma_{MS3}^2 = 4\sigma_{SS1}^2, \quad (5b)$$

$$\sigma_{MS7}^2 = \sigma_{SS4}^2, \quad (5c)$$

where Eq. (5c) is introduced by Rossi *et al.*, despite the fact that this is derived for the cases in which the atoms are aligned, that is, with an angle of 180°, while in the MS7 path, the angle M–N–C is in the range 161°–163°.

The results of the experimental fits are illustrated in Table III. At first sight, it is surprising that some single backscattering path DW factors (SS1 and SS2) at 80 K are larger than those at 300 K, where thermal agitation is higher. Also, in some cases, there are fitted DW factors, whose value is 0, as is the case of the MS4 and MS5 paths for CuPc at 80 K. This makes no sense since the DW factor for the SS paths that involves second and third coordination shells are different from 0, so, the same is expected for the MS paths that involve the second and third coordination shells. This issue will be discussed later.

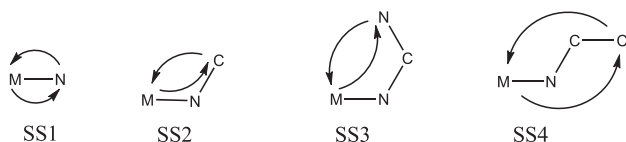
#### B. Molecular dynamics simulations results

##### 1. Average structures from MD simulations: Testing the original force field

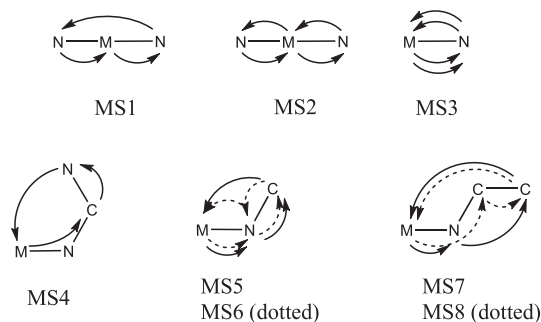
Table IV collects the average distances, obtained from the MD simulations at 80 K, from the central zinc atom to the different coordination shells. The force field used is the one published by Dwyer *et al.*,<sup>27</sup> which from now on will be labeled as “original FF.” Those results are compared with the experimental ones, obtained from the fitting of the EXAFS spectrum reported by Rossi *et al.*,<sup>20</sup> and from the QM optimization at the MP2 level. Differences between the original FF and the experimental results are typically about 0.05 Å.

In Fig. 4, the average theoretical ZnPc EXAFS spectrum, based on the original FF simulation, has been represented to check if it

#### Single Scattering (SS) Paths



#### Multiple Scattering (MS) Paths

**FIG. 3.** Backscattering paths, where M is the absorber atom.

**TABLE III.** Distances and DW factors ( $\sigma^2$ ) obtained from the experimental fittings. DW factors are multiplied by a factor  $10^3$ .

Path	FePc 80 K <sup>20</sup>		NiPc 300 K <sup>21</sup>		CuPc 80 K <sup>20</sup>		CuPc 300 K <sup>19</sup>		ZnPc 80 K <sup>20</sup>	
	R (Å)	$\sigma^2$ (Å <sup>2</sup> )	R (Å)	$\sigma^2$ (Å <sup>2</sup> )	R (Å)	$\sigma^2$ (Å <sup>2</sup> )	R (Å)	$\sigma^2$ (Å <sup>2</sup> )	R (Å)	$\sigma^2$ (Å <sup>2</sup> )
SS1	1.9325(0.0073)	5.8	1.90(0.02)	4	1.945(0.006)	3.06	1.95(0.01)	0.8	2.0023(0.0079)	6.1
SS2	2.968(0.011)	5.6	2.90(0.09)	7	2.973(0.009)	2.5	2.97(0.02)	2	3.029(0.012)	6.0
SS3	3.378(0.013)	5.4	3.29(0.03)	1	3.38(0.01)	2.8	3.37(0.02)	4	3.418(0.014)	8.4
SS4	4.203(0.016)	9.4	4.31(0.06)	1	4.22(0.01)	6.3	4.1(0.1)	7	4.275(0.017)	7.8
MS1		11.6				6.12		1.6		12.2
MS2		11.6				6.12		1.6		12.2
MS3								3.2		
MS4		1.4				0				3.1
MS5		1.3				0		16		2.8
MS6								16		
MS7		9.4				6.30		10		7.8
MS8		26				33		10		17

reproduces the main features of the experimental one. Despite its complexity, we see that the oscillations of the experimental spectrum and their positions are largely reproduced. Nonetheless, despite the overall good reproduction, there are regions that can be improved.

The origin of these discrepancies can be twofold: On one hand, the structural differences observed in [Table IV](#) are significant enough to show up in the comparison of the spectra, and, on the other hand, there are significant deviations produced by the DW factors associated with each of the contributions. Therefore, with the aim of improving the reproduction of the experimental spectra, the original force field has been modified. Only some equilibrium distances have been changed in the corresponding bond-stretching contributions and one of the angles in order to reduce the discrepancies present in [Table IV](#). This new force field is called “modified FF.” The modifications introduced were illustrated in [Table II](#). The last column of [Table IV](#) collects the average distances obtained from the modified FF simulation. To change the DW factors, it would be necessary to modify the effective force constants acting between bonded atoms, which is an involved task in the case of such a complicated system.

The MD simulation with the modified FF yields structural results in which the theoretical–experimental agreement is clearly improved. The lower part of [Fig. 4](#) shows the spectra obtained after the modifications made in the original FF. It is evident that the

**TABLE IV.** Average distances (Å) for the first four shells of ZnPc from MD simulations, from experimental EXAFS fitting, and from the MP2 optimization.  $R_n$ , with  $n = 1, 2, 3, 4$ , are the distances from the metal to the first, second, third, and fourth coordination shells, represented in [Fig. 1](#).

	Original FF <sup>27</sup>	Experimental <sup>20</sup>	MP2	Modified FF
$R_1$	1.947	$2.0023 \pm 0.0079$	1.985	1.985
$R_2$	2.970	$3.029 \pm 0.012$	2.997	2.996
$R_3$	3.339	$3.418 \pm 0.014$	3.390	3.390
$R_4$	4.220	$4.275 \pm 0.017$	4.240	4.241

average spectrum obtained from the modified FF improves most of the deficiencies observed in the case of the original one. The main differences are highlighted with dotted ellipses.

The different periodic functions contributing to  $\chi(k)$  depend on the path lengths and, therefore, on distances between the back scatterers, as can be seen in [Eq. \(3\)](#). In turn, in this case, the rigidity of the molecule makes relevant a multitude of contributions with different frequencies and phases, which creates a very complex spectrum. That is the reason why small structural modifications, such as those shown in [Table II](#), give rise to significant changes in the spectrum—due to interference phenomena. In a more labile system, this effect would be much less intense.

## 2. Convergence of the theoretical spectra with the number of shells and legs

[Figures 5](#) and [6](#) show the evolution of the average spectrum of ZnPc with the increase in the number of shells around the absorber atom and with the number of scattering path legs. The analysis is done for Zn, but results can be extrapolated to the rest of the complexes.

In the generation of the spectra by shells ([Fig. 5](#)), the number of legs was enough, so, this parameter does not influence the analysis. Convergence is reached when a total of five shells around the absorbing atom are considered.

[Figure 6](#) shows the evolution of the spectrum shape when considering backscattering paths with an increasing number of legs. Now, a sufficient number of shells around the absorbing atom have been considered, so that this parameter does not interfere in the analysis of the number of legs. In this case, convergence is achieved by considering paths up to six legs.

The evolution of both sets of spectra does not show a clear pattern, reflecting complex contributions when gradually increasing each of the parameters analyzed. It is interesting to note the simplicity of the EXAFS  $\chi(k)$  function when considering SS and MS paths of only the first shell, defined by the four nitrogen atoms bonded to the metal (see top of [Fig. 5](#)). In this case, the predominant contribution comes from the simple Zn–N backscattering path and does not account for the shape of the spectrum. In contrast, the first spectrum

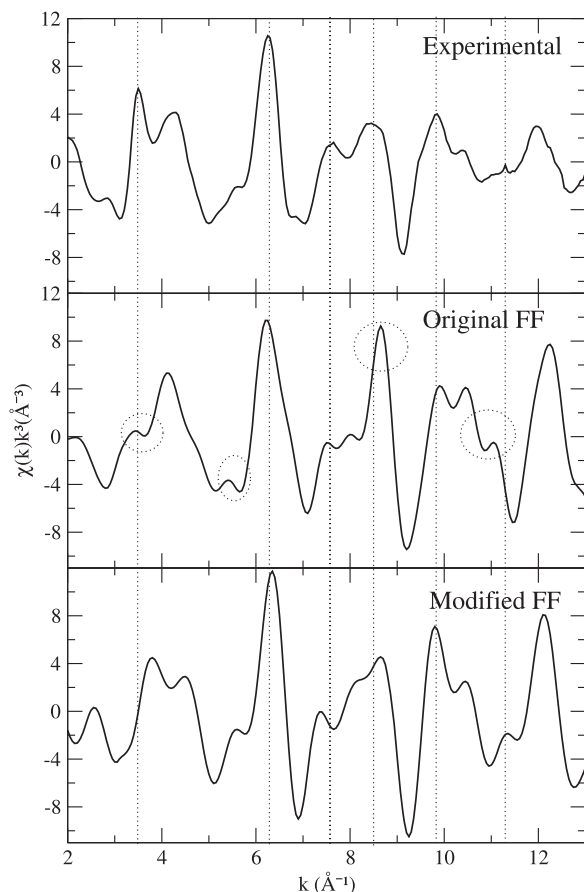


**FIG. 4.** ZnPc EXAFS spectra. On top, the experimental one published by Rossi *et al.*,<sup>20</sup> in the middle, the average EXAFS spectrum obtained from the original FF,<sup>27</sup> and at the bottom, the average EXAFS spectrum obtained from the modified FF. The dotted vertical lines and ellipses serve as a visual aid to facilitate comparisons.

in Fig. 6, in which only the SS paths are considered, already presents a structure far from simple, capturing to a large extent the global complexity of the spectrum. It is worth noting in this case, that the pattern observed is the result of superimposing the SS contributions corresponding to successive coordination shells around the central metal ion, each of them with significantly different distances.

The results presented are completely compatible with the conclusions presented by Carrera *et al.*<sup>19</sup> and Rossi *et al.*<sup>20</sup> in their respective studies. In the first case, Carrera *et al.*, in their analysis of the Fourier transform of the EXAFS spectrum of CuPc at 300 K, confirm that the signal beyond 4 Å is still intense enough to require the inclusion of the fifth (5.5 Å) and sixth (6.5 Å) shells in the analysis. However, taking into account these shells in their analysis would mean a large increase in the number of parameters to fit, since 42 new MS paths would appear, with an intensity greater than 10%,<sup>19</sup> making fitting nonfeasible. Rossi *et al.* come to a similar conclusion, but in this case analyzing the XANES spectra instead of EXAFS. According to them, six shells would be necessary to grasp all the features observed in the experimental spectra.

## SHELLS

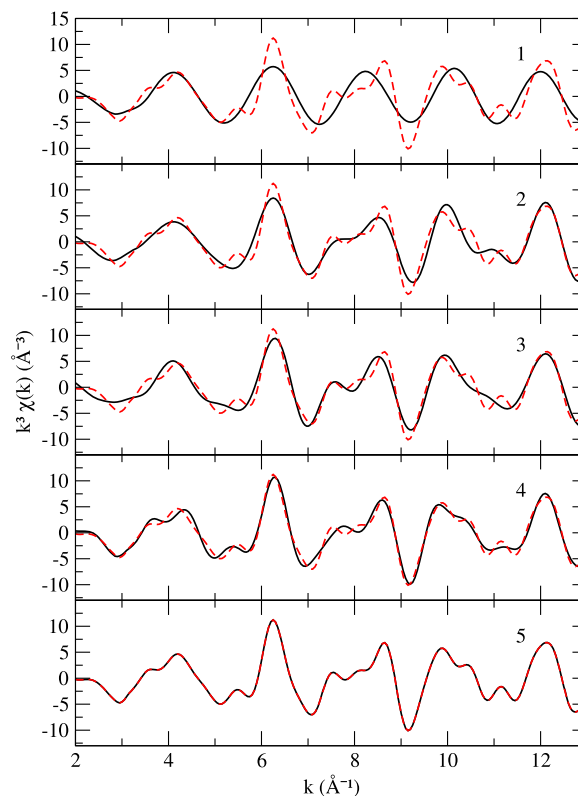


**FIG. 5.** Evolution of the average ZnPc spectra at 80 K, as the number of shells increases. The final converged spectrum (obtained with six shells and paths with seven legs) is shown as a dashed line to facilitate comparison.

### 3. Extension to other MPCs

Due to the clear improvement obtained in Sec. III B 1, with the modification of the FF published by Dwyer *et al.*,<sup>27</sup> we propose the extrapolation of this methodology to other MPC complexes. Those metals are Fe, Ni, and Cu, since they belong to the same transition series, and their experimental EXAFS spectra are available.

In Table V, we present the average distances obtained for the MD simulations, the experimental ones, and the QM-optimized geometries at the MP2 level corresponding to the four MPCs studied. The BOMD results are also summarized, but they will be discussed in Sec. III C.

On one hand, MP2 distances are quite close to those provided by the experimental EXAFS fittings. On the other hand, it can be seen that the average distance of the first four shells for the classical MD fully reproduces the results of the quantum optimizations, as intended.

The experimental and theoretical MD-based spectra are compared in Fig. 7. We can see that there is an excellent reproduction of the experimental spectra's main features and their positions, especially in the case of NiPc and CuPc, at both temperatures—80 and 300 K. It is worth mentioning that the amplitude of the theoretical

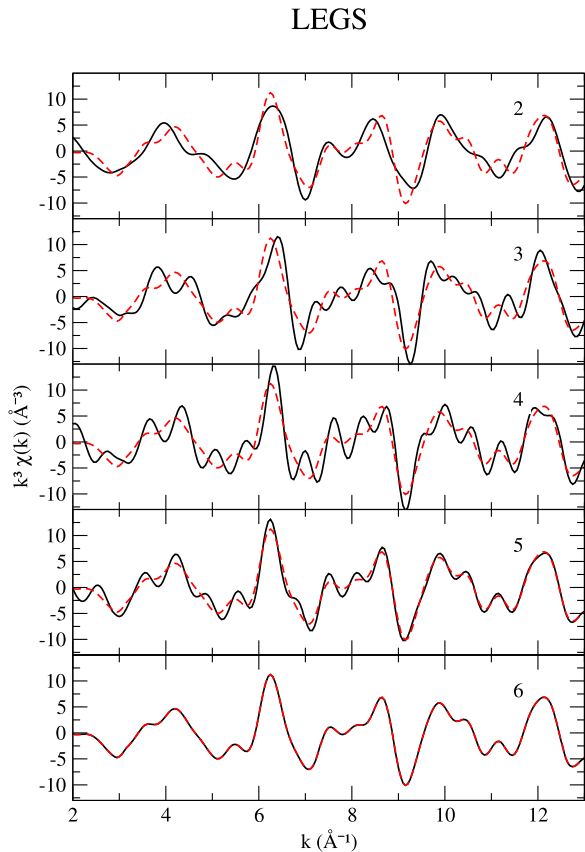


**FIG. 6.** Evolution of the average ZnPc spectra at 80 K, as the number of legs increase. The final converged spectrum (obtained with six shells and paths with seven legs) is shown as a dashed line to facilitate comparison.

spectra of FePc and ZnPc at high  $k$  values is clearly larger than the experimental one, which does not occur in the rest of the species. In the case of FePc, if the experimental spectrum is compared with the experimental spectra of the other MPcs, it is observed that its amplitude is significantly lower at high  $k$  values. In the works of Kim *et al.*<sup>47</sup> and Choi *et al.*,<sup>48</sup> EXAFS spectra of related iron (II) phthalocyanines were recorded, obtaining a slightly higher amplitude at high  $k$  than the one reported by Rossi *et al.*<sup>20</sup>

The contributions and the amplitude of the total spectra will be discussed in the following sections.

### C. Born-Oppenheimer molecular dynamics simulations results

The advantage of BOMD simulations over classical MD simulations is that they do not need to use any force field. After checking that the quality of the level of theory used for BOMD is comparable to the MP2 results, we can use the quantum results as a double check for the quality of our force fields. The differences in shell distances, reported in Table V, between classical MD and BOMD, are typically in the hundredth of Å. To see if there are significant differences in the average EXAFS spectra from classical MD and BOMD simulations, we plot them in Fig. 8.

Although there are slight differences between the two theoretical spectra for each species, the main spectral features are in the same positions and with very similar amplitudes. The largest coincidence in the shell distances between the classical MD and BOMD simulations is found in the FePc. In this case, both theoretical spectra exactly match. In the rest of the MPcs, classical MD and BOMD simulations give slightly different spectra, but they are not so relevant because they hardly affect positions and amplitudes of the spectral features. Therefore, the small differences between both theoretical spectra can be attributed, in this case, either to the different simulation times (5 ps vs 1 ns) or to the different DW factors obtained from each simulation type.

**TABLE V.** Average distances for the first four shells of MPC from MD and BOMD simulations, experimental results from EXAFS fitting, and MP2 optimizations.

		FePc 80 K	NiPc 300 K	CuPc 80 K	CuPc 300 K	ZnPc 80 K
$R_1$ (Å)	MD	1.936	1.888	1.946	1.946	1.985
	BOMD	1.933	1.899	1.959	1.959	1.996
	Exptal.	1.9325	1.90	1.945	1.95	2.0023
	MP2	1.936	1.888	1.946	1.946	1.985
$R_2$ (Å)	MD	2.967	2.934	2.972	2.972	2.996
	BOMD	2.975	2.944	2.985	2.983	3.011
	Exptal.	2.968	2.90	2.973	2.97	3.029
	MP2	2.966	2.934	2.971	2.971	2.997
$R_3$ (Å)	MD	3.377	3.364	3.379	3.379	3.390
	BOMD	3.381	3.361	3.386	3.382	3.396
	Exptal.	3.378	3.29	3.38	3.37	3.418
	MP2	3.377	3.363	3.379	3.379	3.390
$R_4$ (Å)	MD	4.207	4.173	4.214	4.214	4.241
	BOMD	4.209	4.179	4.225	4.222	4.252
	Exptal.	4.203	4.31	4.22	4.1	4.275
	MP2	4.207	4.174	4.213	4.213	4.240



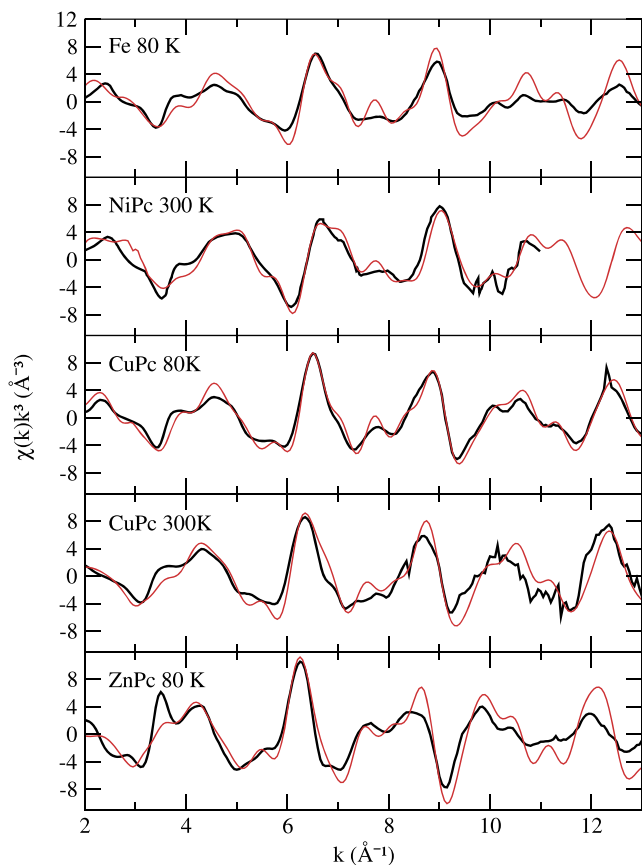


FIG. 7. EXAFS spectra, theoretical (classical MD), in red, and experimental, in black.

#### D. Temporal convergence of the theoretical spectra

Due to the high computational cost of BOMD simulations, we have a production time of only 5 ps. In contrast, classical molecular dynamics simulations can produce long production times. With the help of classical MD simulations, we can study the temporal convergence of the EXAFS spectra. In Fig. S1 in the [supplementary material](#), the average EXAFS spectra of MPCs computed for structures extracted from 5 ps to 1 ns of classical MD simulations are plotted. Both of them are computed with the same number of snapshots and with the same parameters ( $S_0^2, E_0$ ). There is almost no difference between them. We can safely consider then that 5 ps of simulation is enough to have a converged EXAFS spectrum, validating, therefore, the BOMD spectra already presented.

#### E. Debye–Waller factor analysis

##### 1. Results from MD simulations

The complexity of fitting the EXAFS spectra of the MPCs has its origin in their high molecular rigidity, which makes it necessary to take into account a large number of contributions. This causes the fitting of the DW factors associated with each backscattering path

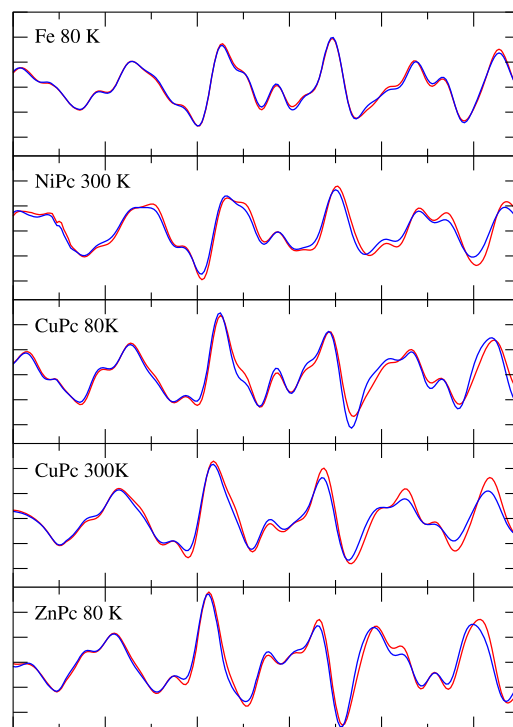


FIG. 8. Theoretical EXAFS spectra (classical MD in red, and BOMD in blue).

more difficult to do, since they are strongly correlated with other parameters that affect the amplitude.<sup>45</sup>

Due to the exponential character of the term that contains the DW factor in the EXAFS equation, the precision in its determination is crucial for making a quantitative analysis of the spectrum. In fact, its determination is a limiting factor when making structural characterizations, since it affects the amplitude of the signal related, for example, to the coordination number around the absorbing atom. In our system, that parameter is known, but this is not the case in many other systems, with ligands that have low residence times in the absorber environment. In addition, it is strongly correlated with the amplitude reduction factor  $S_0^2$ , so, its theoretical estimation supposes a great improvement in the fitting and in the reduction of the number of free parameters during the fitting process.<sup>43</sup>

The strategy that followed the experimental studies of Rossi *et al.*<sup>20</sup> and Carrera *et al.*<sup>19</sup> was to relate some of the DW factors of the MS paths with those of SS through simple formulas, as discussed in the Methodology section. These approximations imply a reduction in the number of free parameters to fit. However, both studies differ in the selection of backscattering paths, as well as in some of the expressions that relate the DW factors of the different contributions. Those facts simply illustrate the complexity of the analysis.

We can calculate directly the DW factor for every scattering path in our simulation. For the aim of comparison, we have computed the DW factors of the scattering paths employed in the fitting process of Refs. 19 and 20 and schematized in Fig. 3. Figure 9 shows the theoretical and the experimentally fitted DW factors. First, we

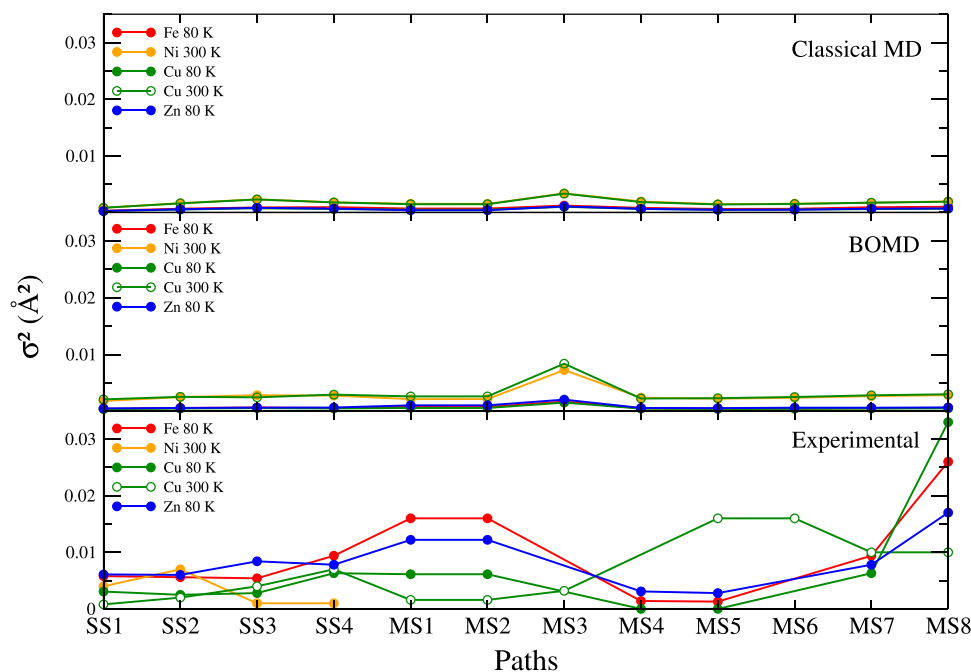


**FIG. 9.** Debye–Waller factors calculated for the classical MD and BOMD and their comparison with the fitted experimental values.

can see that the differences between the DW factors of both MD simulations and those experimentally fitted can be as high as one order of magnitude. Also, in some cases, there are fitted DW factors whose value is 0, such as in the case for MS4 and MS5 paths for CuPc at 80 K, as stated in a Sec. III A. This shows some degree of inconsistency in the analysis of the experimental spectra.

When comparing both MD simulations—classical and Born–Oppenheimer—we can see that the differences are smaller (all in the same order of magnitude) and follow the same trend. The values are summarized in Table VI. BOMD DW factors are on average, a bit larger than the MD ones, with a maximum

$\sigma_{\text{BOMD}}^2/\sigma_{\text{MD}}^2$  ratio of 2.5 for just a few cases. Even though there are differences between the values of the DW factors of both theoretical simulations, these are not reflected in the average EXAFS spectra, because there are so many contributions to the total simulated spectra that the differences are diluted (see Fig. 8).

As stated before, the DW factor accounts for the disorder around the absorber atom. We can visualize the trajectories that follow the atoms in both types of MD simulations. The trajectory of ZnPc atoms in the classical MD simulation is represented in Fig. 10. An equivalent representation for the BOMD simulation is included in the supplementary material (Fig. S2). In both cases, the

**TABLE VI.** DW factors ( $\text{\AA}^2$ ) of MD simulations multiplied by a factor  $10^3$ .

Path	FePc 80 K		NiPc 300 K		CuPc 80 K		CuPc 300 K		ZnPc 80 K	
	MD	BOMD	MD	BOMD	MD	BOMD	MD	BOMD	MD	BOMD
SS1	0.309	0.428	0.843	1.82	0.250	0.384	0.837	2.10	0.269	0.514
SS2	0.674	0.581	1.653	2.50	0.531	0.490	1.617	2.55	0.574	0.590
SS3	0.895	0.664	2.321	2.83	0.750	0.562	2.304	2.46	0.832	0.656
SS4	0.952	0.577	1.803	2.77	0.614	0.494	1.783	2.93	0.691	0.658
MS1	0.706	0.774	1.539	2.15	0.489	0.589	1.474	2.62	0.411	1.05
MS2	0.705	0.774	1.536	2.16	0.489	0.591	1.477	2.62	0.411	1.05
MS3	1.236	1.71	3.371	7.26	1.001	1.54	3.349	8.38	1.076	2.06
MS4	0.819	0.549	1.954	2.40	0.643	0.462	1.850	2.25	0.647	0.590
MS5	0.632	0.470	1.464	2.22	0.480	0.407	1.419	2.31	0.487	0.556
MS6	0.666	0.488	1.556	2.38	0.515	0.443	1.520	2.51	0.490	0.633
MS7	0.935	0.547	1.747	2.67	0.596	0.482	1.733	2.82	0.669	0.640
MS8	1.013	0.616	1.975	2.84	0.676	0.508	1.911	2.99	0.723	0.678

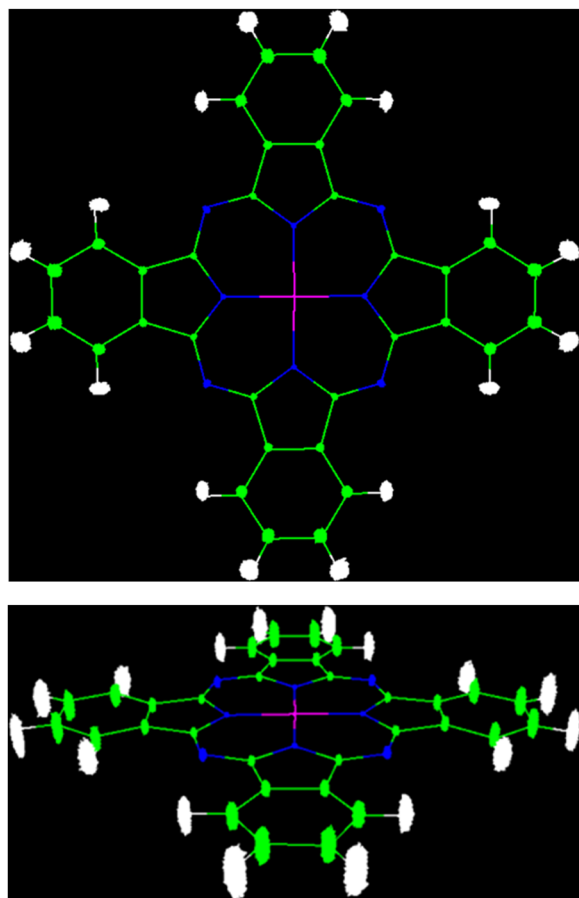


**FIG. 10.** Representation, axial and equatorial views, of the trajectory followed by the atoms in the classical MD simulation of ZnPc at 80 K. Equivalent results are obtained in BOMD simulations (Fig. S2 in the [supplementary material](#)).

oscillations of the atoms are much larger in the axis perpendicular to the molecular plane. In addition, atoms' trajectories follow a “banana” shape, shown in Fig. 11, especially appreciable in the BOMD trajectory. Thus, the absorber–backscatter distances do not change noticeably because they follow paths close to an arc of a circumference. This motion is not reflected in the SS DW factors, which account for the differences in the radial distances from the absorber to the backscatter atoms.

We can see this phenomenon through numbers. In Fig. 12, we plot, grouped by shells, the calculated variance of the  $x$ ,  $y$ , and  $z$  components around the average position for all the atoms in the ZnPc simulations (both classical MD and BOMD), the molecule being in the  $xy$  plane and the metal ion at the origin of the coordinate system. The variance is more than ten times larger for the  $z$  axis contribution than for the  $x$  or  $y$  ones. This fact stands out especially in the case of BOMD, where the deformations increase considerably in the farthest shells. The value of the variance for the total distance  $r$  (DW factor in single scattering paths and shown in Fig. 12 as well) is closer to the deviations in the  $x$  and  $y$  axes. Thus, the oscillations that do not change significantly with the absorber–backscatter distance are not

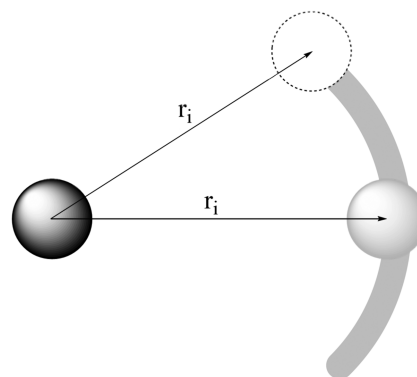


**FIG. 11.** Representation of the backscatter atom movement following a banana shape. The shaded line represents the radial amplitude of the motion.

reflected in the DW factors. The result is equivalent for the rest of the MPcs.

The underestimation of DW factors would lead to an increase of the EXAFS signal, which we may be compensating for with small  $S_0^2$  values (Table S2 in the [supplementary material](#)). However, for the CuPc at 300 K and ZnPc at 80 K cases, the  $S_0^2$  value used for the theoretical spectra is 1, so, despite having much smaller DW factors than those fitted experimentally, we get EXAFS spectra with the same amplitudes than the experimental ones. This fact can be again a proof of the effect of the interference pattern generated when *all* the scattering path contributions are included in the generation of the EXAFS spectra. That is, the lack of scattering paths included in the fitting of the experimental information can be compensated with higher DW factors. In the cases of FePc and ZnPc, as mentioned, we still have problems of higher amplitudes at high  $k$  values in the theoretical spectra despite the fact that the amplitude of the spectra fit well at low  $k$ , either with the use of a small  $S_0^2$  (FePc) or not (ZnPc).

There are unresolved issues concerning the amplitude of EXAFS spectra: It is not clear why in some cases the intensity matches the experimental ones and in others it does not. Factors such as the extraction and analysis of the raw data and possible self-absorption problems,<sup>49</sup> should be considered and analyzed.

## 2. Analyzing DW factor relationships applied in the experimental fittings

We can also check if the relationships between the DW factors of SS and MS applied by Carrera *et al.*<sup>19</sup> and Rossi *et al.*<sup>20</sup> [Eq. (5)] are reproduced by simulations. Table VII collects the computed relationships from our simulation results.

In order to apply the independent vibration model in the experimental fittings, two premises must be met: the thermal motion of the atoms in the direction perpendicular to the bond must be small compared to the bond distance, and the movement must not be correlated,<sup>50</sup> that is, the oscillations of the atoms are not influenced by the oscillations of other atoms.

First, classical MD and BOMD simulation results differ and do not follow a clear trend. We can observe that the first two relationships, which involve the MS1, MS2, and SS1 paths, have a maximum deviation close to 40%. These paths involve the central metal and its four-nearest nitrogen atoms. The origin of the discrepancies

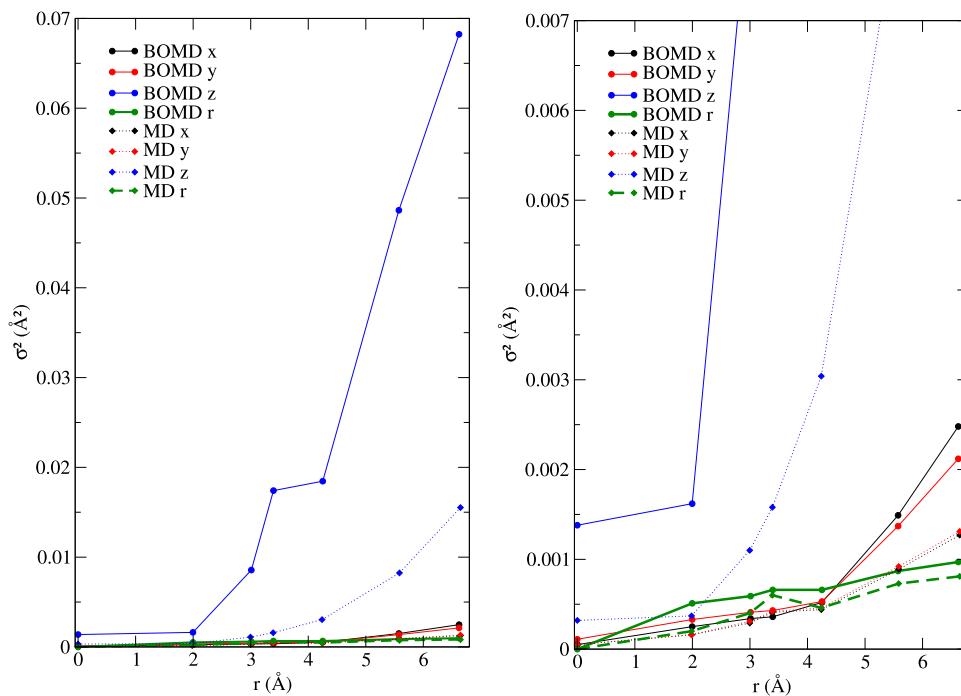


**FIG. 12.** Representation of the variance around the average position for each shell for both classical and BOMD simulations of ZnPc. On the left, the whole graphic, on the right, a zoom  $\times 10$  in the vertical axis.

between the value expected from the independent vibration model and the values extracted from simulations leads us to think that the independent vibration model is a rough approach in the case of MS paths that involve the closest shell to the metal. This fact makes sense, considering that phthalocyanine is a single tetradentate and aromatic (and, therefore, rigid) ligand. We can think that the movements of the nitrogen atoms that bind the metal are correlated since they are subject to the influence of the ring, which is a single entity. This hypothesis is supported by the study done by Z. Liu *et al.*<sup>51</sup> on the vibrational structure of MPcs. According to them, all normal modes above  $955\text{ cm}^{-1}$  are mainly involved in

in-plane bending (IPB) vibrations, and it is difficult for a bond to vibrate without involving other bonds for such a macrocyclic ring. Furthermore, IPB is the kind of vibration that “appears” when calculating the DW factors, as mentioned before. Anyhow, the imposed ratios in the experimental analysis are, in all cases, very reasonable approximations.

In the last relationship [Eq. (5c)], which involves paths MS7 and SS4, the equivalence is essentially fulfilled. The movement of the four different atoms that involve the MS7 paths may be decorrelated enough to fulfill the conditions needed to apply the independent vibration model.

To understand why the relationship between MS3 and SS1 is fulfilled in all cases, we have to go through the equation we use to calculate the DW factor. For the SS1 path, it would be

$$\sigma_{\text{SS1}}^2 \equiv \left\langle \left( \frac{\vec{r}_i - \vec{r}_0 + \vec{r}_i - \vec{r}_0}{2} \right)^2 \right\rangle_i = \langle (\vec{r}_i - \vec{r}_0)^2 \rangle_i, \quad (6)$$

where  $\vec{r}_0$  is the equilibrium distance from the absorbing atom to the backscatter, and  $\vec{r}_i$  is the instantaneous position of the backscatter atom, as illustrated in Fig. 13. For the case of the MS3 path,  $\sigma_{\text{MS3}}^2$  would be calculated as

$$\begin{aligned} \sigma_{\text{MS3}}^2 &\equiv \left\langle \left( \frac{\vec{r}_i - \vec{r}_0 + \vec{r}_i - \vec{r}_0 + \vec{r}_i - \vec{r}_0}{2} \right)^2 \right\rangle_i, \\ &= \left\langle \left( \frac{4\vec{r}_i - 4\vec{r}_0}{2} \right)^2 \right\rangle_i \equiv 4\sigma_{\text{SS1}}^2. \end{aligned} \quad (7)$$

Thus, by definition,  $\sigma_{\text{MS3}}^2/\sigma_{\text{SS1}}^2$  is always fulfilled.

**TABLE VII.** Calculation of the relationships between the theoretical Debye–Waller factors. The last row corresponds to the approximations imposed in the experimental fittings.

System		$\frac{\sigma_{\text{MS1}}^2}{\sigma_{\text{SS1}}^2}$	$\frac{\sigma_{\text{MS2}}^2}{\sigma_{\text{SS1}}^2}$	$\frac{\sigma_{\text{MS3}}^2}{\sigma_{\text{SS1}}^2}$	$\frac{\sigma_{\text{MS7}}^2}{\sigma_{\text{SS4}}^2}$
FePc 80 K	MD	2.28	2.28	4.00	0.98
	BOMD	1.81	1.81	4.00	0.95
NiPc 300 K	MD	1.83	1.82	4.00	0.97
	BOMD	1.68	1.68	4.00	0.96
CuPc 80 K	MD	1.95	1.95	4.00	0.97
	BOMD	1.53	1.54	4.00	0.97
CuPc 300 K	MD	1.76	1.76	4.00	0.97
	BOMD	1.25	1.25	4.00	0.96
ZnPc 80 K	MD	1.53	1.53	4.00	0.97
	BOMD	2.05	2.04	4.00	0.97
Imposed		2	2	4	1

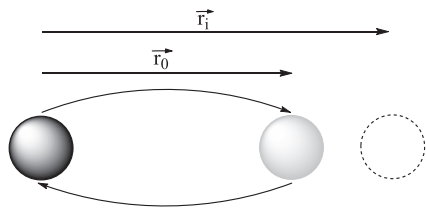


FIG. 13. Single scattering path, indicating instantaneous  $\vec{r}_i$  and equilibrium  $\vec{r}_0$  distances.

## F. EXAFS spectra with a reduced number of paths

### 1. Testing the model structure concept

One option at this point is to compare the “complete” average theoretical spectra with the spectra calculated taking into account only the paths included in the fittings of experimental spectra. However, before addressing this issue, an interesting question within the fitting process of an experimental spectrum will be considered. In the fitting of experimental spectra, a model structure is adopted that essentially determines the contributions to the final spectrum. As already mentioned, the fitting of the spectra provides, basically, the distance of the backscattering atoms and the static and dynamic disorder that they exhibit. This disorder is reflected in the DW factor associated with each group of backscattering paths.

With the available structural information, we can answer the following question: Is an average spectrum, taking into account only certain backscattering paths, equivalent to a single spectrum based on a model structure considering the same paths through their extracted DW factors from the simulation? In the first case, the average spectrum is built from the structures extracted from the MD simulations, incorporating in each of them only the set of selected backscattering paths. In the second case, a single spectrum is generated on the basis of a single (model) structure, also selecting the same paths as in the first case and introducing the disorder through the DW factors resulting from the MD simulations. In other words, we are asking about the equivalence of Eqs. (1) and (3).

Figure 14 answers the question posed. It compares the spectrum obtained from the statistical average of individual spectra incorporating only the backscattering paths used in the experimental study of Rossi *et al.*<sup>20</sup> and the single spectrum obtained by selecting the same paths for the average structure of the simulation and with the DW factors obtained theoretically. Modified FF at 80 K for ZnPc is chosen as the test case. Equivalent results must be expected for the other MPcs.

It is interesting to see how the same results can be reproduced from a single spectrum, without the need to generate a spectrum for each snapshot of the MD trajectory. This strategy entails lower computational cost, although the *a priori* knowledge of the main contributions (paths) becomes compulsory. It should be noted that the intrinsic rigidity of the studied system greatly favors the equivalence between both strategies. It would be interesting to do this comparison in coordination environments with a greater degree of flexibility or in more disordered systems.

### 2. Average EXAFS spectra selecting paths

To shed light on the origin of the differences between the theoretical and experimental DW factors, average EXAFS spectra have

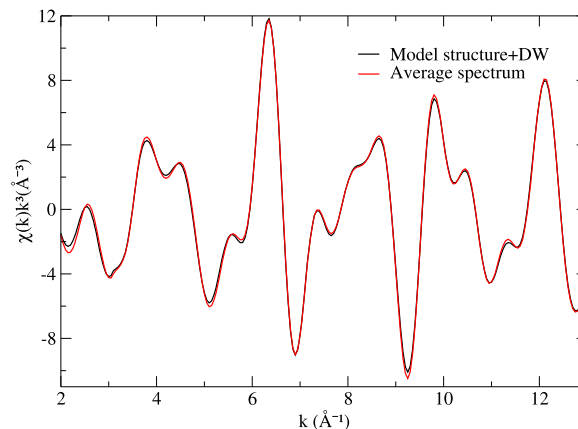


FIG. 14. Average EXAFS spectrum (in red) obtained from ZnPc MD simulation at 80 K, including only the scattering paths considered by Rossi *et al.*<sup>20</sup> In black, EXAFS spectrum obtained by employing the average structure (model structure) and considering the same paths whose DW factors are extracted from the same simulation.

been generated using only the paths that the experimental analyses considered in their fits.

In Fig. 15, we plot the total average (converged) spectra obtained from classical MD simulations and the average spectra

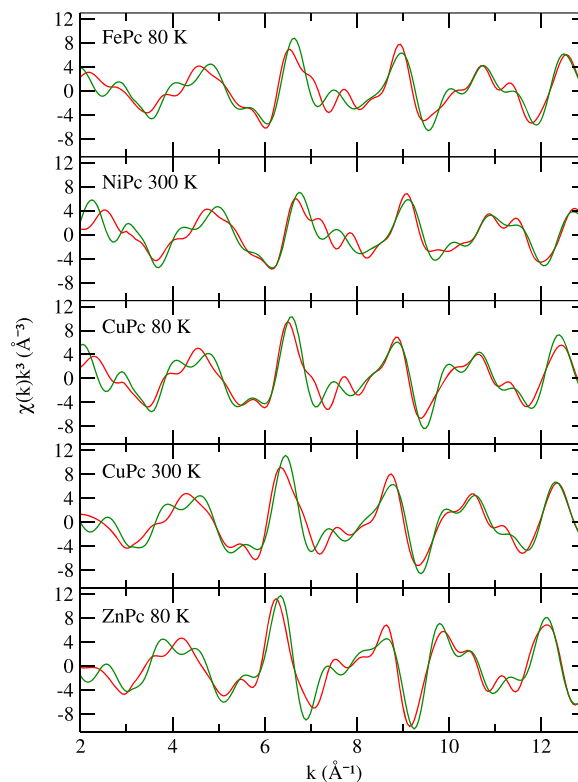
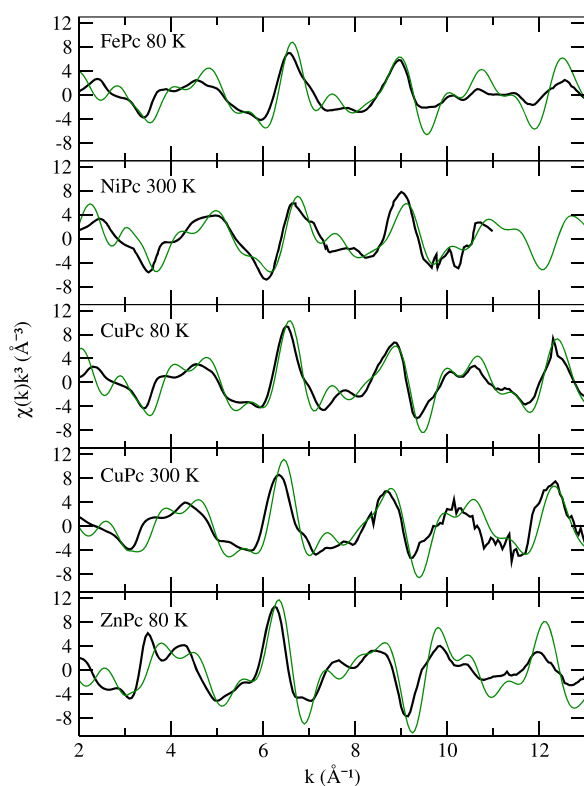


FIG. 15. Average EXAFS spectra selecting paths (green) vs total average EXAFS spectra for classical MD simulations (red) (Fig. S4 in the [supplementary material](#) shows the equivalent plot for BOMD simulations).

including only the paths used in the work of Rossi *et al.*<sup>20</sup> It is shown in Fig. S3 in the [supplementary material](#) that the results are equivalent if the path selection of Carrera *et al.*<sup>19</sup> is considered. Although for both classical MD and BOMD, some of the main features are present, such as the peaks at 6 and 8–9  $\text{\AA}^{-1}$ , there are regions that remain incomplete. That is, the average spectra with the selected paths are not “converged.” In Fig. 16, we plot the average EXAFS spectra, only including the selected paths and the experimental ones. If we compare Fig. 7 with Fig. 16, the low  $k$  region gets considerably worse when going from the “total” spectrum to the spectrum generated with the mentioned path selection. In this region, MS paths are especially relevant. There are also appreciable differences in the 7–9  $\text{\AA}^{-1}$  region. When we generate the theoretical EXAFS, for a symmetric structure, there are around 300 paths (not counting degeneracy) that contribute to the final spectrum. In the experimental fittings, however, the contribution of only 10–12 paths is taken into account. The lack of paths considered in the fit may be compensated by larger DW factors, leading, at least partially, to the observed differences between the theoretical results and the experimental fits (Fig. 9). It is important to note that 10–12 paths supposes, in this case, around 60 contributions to the total spectrum because of the intrinsic degeneracy of some of the paths.

Making experimental fittings without knowing *a priori* how many paths are necessary and their relevance is an extremely difficult



**FIG. 16.** Average EXAFS spectra selecting paths for classical MD simulations (green) vs experimental EXAFS spectra (black) (Fig. S5 in the [supplementary material](#) shows the equivalent plot for BOMD simulations.).

task. In other types of systems, as in the case of ions in solution or small molecules, 10–12 paths would be more than enough, but since any MPc is a very rigid molecule with a considerably high number of atoms, this task becomes too complicated. In this case, the use of theoretical information greatly facilitates the work and leads to more accurate fittings.

#### IV. CONCLUDING REMARKS

The complexity and rigidity of MPcs, together with the sensitivity of EXAFS to minor structural changes, makes this chemical motif a good test-bed for the development of theoretical strategies due to the difficulties appearing in the spectrum fitting. In this sense, this study is a good example of the interplay between theoretical methods and experiment: Experiments provide tools to benchmark theoretical models, and theoretical models allow us to evaluate approximations/simplifications made during the analysis of the experimental information.

The first conclusion is that the experimental ZnPc spectrum is quite well reproduced by employing the original force field. However, some features were lacking in the theoretical spectrum. To improve this situation, an MP2 optimized structure was employed as a reference to introduce some changes in the original ZnPc force field, reaching a better agreement between experiment and theory. This result reveals the sensitivity of EXAFS spectroscopy in the determination of the close environment of the absorber atom. That modified force field was the starting point for the extension of the methodology to other MPcs since structural changes essentially occur in the region close to the metal center.

The evolution of the interference pattern, observed when the number of shells and legs in scattering paths was increased, is involved due to the large number of contributions with different frequencies (a function of the different effective distances) to be considered.

As a check, the results of the BOMD simulations were compared with the results of the classical MD simulations. After verifying that a 5 ps simulation time was enough to have temporarily converged results, we have shown that, with two different computational levels of calculations, equivalent results can be reached.

The goodness of the approximations employed in the experimental analysis to reduce the number of free parameters in the fitting process (relationships between MS and SS DW factors) was checked on the basis of our MD results, concluding that it was reasonable although the MS paths involving the closer atoms to the absorber exhibit higher deviations (vibrations strongly correlated with ring motions).

Taking into account the amplitude of the EXAFS oscillations, it can be concluded that the theoretical DW factors are systematically smaller than the experimental ones. Being aware of the limitations present in the theoretical strategy, the discrepancy between the experimental and theoretical DW factors is partly due to the lack of scattering paths included in the fitting of the experimental spectra (due to the restrictions concerning the number of parameters that can be fitted). This fact is then compensated by higher values of the fitted DW factors in the considered contributions. Nonetheless, there are still unresolved issues related to the intensity of the theoretical EXAFS spectra, such as the high intensity obtained for FePc and ZnPc at high  $k$  values.

It should be noted that, despite these discrepancies, the determination of the distances from the absorber atoms to the backscattering ones are not affected, showing the robustness of the technique to the geometrical information (average distances).

The concept of model structure has been evaluated and, at least in this case, from a theoretical view, it has been possible to check the validity of a computationally less expensive strategy of generating spectra with a previous selection of backscattering paths, that is, without the need for computing average spectra. Whether this strategy is the most straightforward one or not depends on the ability of choosing all the relevant scattering contributions. For the MPC systems, it is shown that this is not the case.

One of the possible steps to follow would be the modification of the effective force constants to give accurate frequencies for the normal modes that involve the metal region. In the work of Z. Liu *et al.*,<sup>51</sup> the tendencies of the different metal-substituted MPCs in molecular, electronic, and vibrational structures are studied. They demonstrated with the assignment of IR and Raman frequencies, that the absorption bands, which are metal dependent, show a definite trend with the variation of the substituted metal, while the rest of the vibrational modes (most of them) do not show significant shifts with the metal ion.

## SUPPLEMENTARY MATERIAL

See the [supplementary material](#) for charges of the force field,  $E_0$ , and  $S_0^2$  for the theoretical EXAFS computation, trajectory of the ZnPc atoms in BOMD simulation, and comparisons of theoretical EXAFS spectra.

## ACKNOWLEDGMENTS

The authors thank Professor Stephen P. Kelty for providing NAMD inputs of the ZnPc FF and Professor Federico Boscherini for the experimental EXAFS data of FePc, CuPc, and ZnPc. This work was the result of the I+D+i research Project No. PGC2018-099366-B-I00, funded by the Ministerio de Ciencia e Innovación, Agencia Estatal de Investigación (DOI:10.13039/501100011033) and by ERDF, a way of making Europe. G.R.H. is grateful for a grant associated with the research Project No. FEDER US-1264472, funded by the Junta de Andalucía and Universidad de Sevilla, and for a Ph.D. scholarship (PIF, VI PPIT-US) from the Universidad de Sevilla.

## AUTHOR DECLARATIONS

### Conflict of Interest

The authors have no conflicts to disclose.

## Author Contributions

**Gema Raposo-Hernández:** Formal analysis (equal); Investigation (lead); Software (equal); Visualization (equal); Writing – original draft (lead). **Enrique Sánchez Marcos:** Funding acquisition (lead); Methodology (equal); Writing – review & editing (equal). **Rafael R. Pappalardo:** Methodology (equal); Software (equal); Writing –

review & editing (equal). **José M. Martínez:** Conceptualization (lead); Methodology (equal); Software (equal); Supervision (lead); Visualization (equal); Writing – review & editing (equal).

## DATA AVAILABILITY

The data that support the findings of this study are available from the corresponding author upon reasonable request.

## REFERENCES

- 1 G. De La Torre, C. G. Claessens, and T. Torres, *Chem. Commun.* **38**, 2000 (2007).
- 2 R. Bonnett, *Chem. Soc. Rev.* **24**, 19 (1995).
- 3 M.-E. Ragoussi, M. Ince, and T. Torres, *Eur. J. Org. Chem.* **2013**, 6475.
- 4 K. R. Venugopala Reddy, J. Keshavayya, and J. Seetharamappa, *Dyes Pigm.* **59**, 237 (2003).
- 5 M. S. Savelyev, A. Y. Gerasimenko, V. M. Podgaetskii, S. A. Tereshchenko, S. V. Selishchev, and A. Y. Tolbin, *Opt. Laser Technol.* **117**, 272 (2019).
- 6 A. Y. Tolbin, M. S. Savelyev, A. Y. Gerasimenko, L. G. Tomilova, and N. S. Zefirov, *Phys. Chem. Chem. Phys.* **18**, 15964 (2016).
- 7 M. Y. Ogawa, J. Martinsen, S. M. Palmer, J. L. Stanton, J. Tanaka, R. L. Greene, B. M. Hoffman, and J. A. Ibers, *J. Am. Chem. Soc.* **109**, 1115 (1987).
- 8 V. Mastryukov, C.-y. Ruan, M. Fink, Z. Wang, and R. Pachter, *J. Mol. Struct.* **556**, 225 (2000).
- 9 C. J. Brown, *J. Chem. Soc. A* **1968**, 2488.
- 10 K. M. Kadish, K. M. Smith, and R. Guilard, *The Porphyrin Handbook* (Elsevier, 2003), Vol. 11, pp. 1–284.
- 11 *Coordination Chemistry of Macrocyclic Compounds*, edited by G. A. Melson (Springer US, Boston, MA, 1979).
- 12 D. K. Cabbiness and D. W. Margerum, *J. Am. Chem. Soc.* **91**, 6540 (1969).
- 13 G. Dufour, C. Poncey, F. Rochet, H. Roulet, S. Iacobucci, M. Sacchi, F. Yubero, N. Motta, M. N. Piancastelli, A. Sgarlata, and M. De Crescenzi, *J. Electron Spectrosc. Relat. Phenom.* **76**, 219 (1995).
- 14 M. Kanai, T. Kawai, K. Motai, X. D. Wang, T. Hashizume, and T. Sakura, *Surf. Sci.* **329**, L619 (1995).
- 15 F. Rochet, G. Dufour, H. Roulet, N. Motta, A. Sgarlata, M. N. Piancastelli, and M. De Crescenzi, *Surf. Sci.* **319**, 10 (1994).
- 16 T. Okajima, H. Fujimoto, M. Sumitomo, T. Araki, E. Ito, H. Ishii, Y. Ouchi, and K. Seki, *Surf. Rev. Lett.* **09**, 441 (2002).
- 17 D. C. Koningsberger and R. Prins, *X-ray Absorption: Principles, Applications, Techniques of EXAFS, SEXAFS, and XANES* (John Wiley and Sons, New York, NY, 1987).
- 18 A. Muñoz-Páez and E. Sánchez Marcos, in *Comprehensive Inorganic Chemistry II*, 2nd ed., edited by J. Reedijk and K. Poeppelemeier (Elsevier, Amsterdam, 2013), pp. 133–159.
- 19 F. Carrera, E. S. Marcos, P. J. Merklings, J. Chaboy, and A. Muñoz-Páez, *Inorg. Chem.* **43**, 6674 (2004).
- 20 G. Rossi, F. d'Acapito, L. Amidani, F. Boscherini, and M. Pedio, *Phys. Chem. Chem. Phys.* **18**, 23686 (2016).
- 21 J. Hong, T. J. Fauvell, W. Helweh, X. Zhang, and L. X. Chen, *J. Photochem. Photobiol., A* **372**, 270 (2019).
- 22 P. J. Merklings, A. Muñoz-Páez, and E. Sánchez Marcos, *J. Am. Chem. Soc.* **124**, 10911 (2002).
- 23 E. C. Beret, K. Provost, D. Müller, and E. S. Marcos, *J. Phys. Chem. B* **113**, 12343 (2009).
- 24 R. Ayala, J. M. Martínez, R. Pappalardo, K. Refson, and E. Sánchez Marcos, *J. Phys. Chem. A* **122**, 1905 (2018).
- 25 S. Pérez-Conesa, J. M. Martínez, R. R. Pappalardo, and E. Sánchez Marcos, *Inorg. Chem.* **57**, 8089 (2018).
- 26 C. Shao, Y. Jin, K. Pipe, M. Shtein, and J. Kieffer, *J. Phys. Chem. C* **118**, 9861 (2014).
- 27 P. J. Dwyer, R. J. Vander Valk, V. Caltaldo, D. Demianicz, and S. P. Kelty, *J. Phys. Chem. A* **118**, 11583 (2014).
- 28 A. J. H. Wachters, *J. Chem. Phys.* **52**, 1033 (1970).

- <sup>29</sup>P. J. Hay, *J. Chem. Phys.* **66**, 4377 (1977).
- <sup>30</sup>K. Raghavachari and G. W. Trucks, *J. Chem. Phys.* **91**, 1062 (1989).
- <sup>31</sup>U. C. Singh and P. A. Kollman, *J. Comput. Chem.* **5**, 129 (1984).
- <sup>32</sup>B. H. Besler, K. M. Merz, Jr., and P. A. Kollman, *J. Comput. Chem.* **11**, 431 (1990).
- <sup>33</sup>J. Tao, J. P. Perdew, V. N. Staroverov, and G. E. Scuseria, *Phys. Rev. Lett.* **91**, 146401 (2003).
- <sup>34</sup>Q. Du, X. Wu, P. Wang, D. Wu, L. Sai, R. B. King, S. J. Park, and J. Zhao, *J. Phys. Chem. C* **124**, 7449 (2020).
- <sup>35</sup>F. Neese, F. Wennmohs, U. Becker, and C. Riplinger, *J. Chem. Phys.* **152**, 224108 (2020).
- <sup>36</sup>I. T. Todorov, W. Smith, K. Trachenko, and M. T. Dove, *J. Mater. Chem.* **16**, 1911 (2006).
- <sup>37</sup>H. J. C. Berendsen, J. P. M. Postma, W. F. Van Gunsteren, A. DiNola, and J. R. Haak, *J. Chem. Phys.* **81**, 3684 (1984).
- <sup>38</sup>G. J. Martyna, M. L. Klein, and M. Tuckerman, *J. Chem. Phys.* **97**, 2635 (1992).
- <sup>39</sup>G. J. Martyna, M. E. Tuckerman, D. J. Tobias, and M. L. Klein, *Mol. Phys.* **87**, 1117 (1996).
- <sup>40</sup>D. E. Sayers, E. A. Stern, and F. W. Lytle, *Phys. Rev. Lett.* **27**, 1204 (1971).
- <sup>41</sup>J. J. Rehr, J. J. Kas, F. D. Vila, M. P. Prange, and K. Jorissen, *Phys. Chem. Chem. Phys.* **12**, 5503 (2010).
- <sup>42</sup>R. Ayala, E. S. Marcos, S. Díaz-Moreno, V. A. Solé, and A. Muñoz-Páez, *The J. Phys. Chem. B* **105**, 7588 (2001).
- <sup>43</sup>K. Provost, E. C. Beret, D. B. Muller, A. Michalowicz, and E. S. Marcos, *J. Chem. Phys.* **138**, 084303 (2013).
- <sup>44</sup>D. Z. Caralampio, J. M. Martínez, R. R. Pappalardo, and E. Sánchez Marcos, *Theor. Chem. Acc.* **136**, 47 (2017).
- <sup>45</sup>T. Yokoyama, K. Kobayashi, T. Ohta, and A. Ugawa, *Phys. Rev. B* **53**, 6111 (1996).
- <sup>46</sup>D. Haskel, "Local structural studies of orientes high temperature superconducting cuprates by polarized XAFS spectroscopy," Ph.D. thesis, University of Washington, Seattle, 1998.
- <sup>47</sup>S. H. Kim, T. Ohta, and G. H. Gang, *Bull. Korean Chem. Soc.* **21**, 588 (2000).
- <sup>48</sup>H. J. Choi, G. Kwag, and S. Kim, *J. Electroanal. Chem.* **508**, 105 (2001).
- <sup>49</sup>G. Raposo-Hernández, J. M. Martínez, R. R. Pappalardo, C. Den Auwer, and E. Sánchez Marcos, *Inorg. Chem.* **61**, 8703 (2022).
- <sup>50</sup>*X-ray Absorption and X-ray Emission Spectroscopy: Theory and Applications*, edited by J. A. Van Bokhoven and C. Lamberti (John Wiley and Sons, Chichester, UK, 2016), Vol. 1–2, pp. 1–845.
- <sup>51</sup>Z. Liu, X. Zhang, Y. Zhang, and J. Jiang, *Spectrochim. Acta, Part A* **67**, 1232 (2007).